Received August 15, 2019, accepted September 12, 2019, date of publication September 17, 2019,
date of current version September 30, 2019.

Digital Object Identifier 10.1109/ACCESS.2019.2941982

Spalling Localization on the Outer Ring of Hybrid Ceramic Ball Bearings Based on the Sound Signals

H. T. SHI[1,2], X. T. BAI[1,2], K. ZHANG[2], Z. N. WANG[1,2], AND Z. M. LIU[1]

[1]School of Mechanical Engineering, Shenyang Jianzhu University, Shenyang 110168, China
[2]Joint International Research Laboratory of Modern Construction Engineering Equipment and Technology, Shenyang Jianzhu University, Shenyang 110168, China

Corresponding author: X. T. Bai (acetyws@163.com)

This work was supported in part by the National Key Research and Development Plan under Grant 2017YFC0703903, and in part by the National Natural Science Foundations of China under Grant 51675353, Grant 51705341, and Grant 51905357.

ABSTRACT Spalling is one of the main defects of hybrid ceramic bearings, and the localization of the spalling is hard to realize based on traditional vibration signals. This paper proposes a new localization method for spalling on the outer ring of hybrid ceramic ball bearings based on the characteristics in the sound radiation signals. The dynamic model containing the spalling is presented, and the sound radiation is obtained through the sub-source decomposition method. Cases when the spallings are located in different zones on the outer ring are studied, and the circumferential distribution of the sound radiation is analyzed in time domain and frequency domain. The localization accuracy with different indicators are compared as well as the recognition clarity, and the results are verified through experimental investigations. Results show that the spalling makes great impact on the sound radiation of the hybrid ceramic ball bearing, and the circumferential and radial distribution of the sound radiation is closely related with the location of the spalling. It is quite essential to acquire the changes of the frequency components in the sound radiation, and the radial attenuation of the amplitude of the spalling-related frequency is crucial for the accurate localization of the spalling.

INDEX TERMS Hybrid ceramic ball bearing, spalling localization, status monitoring, sound signals.

I. INTRODUCTION

The development of technology makes the working conditions of rotating machines more complicated, and brings more critical requirements to the performance of bearings. The hybrid ceramic ball bearings have rings made of steel and balls made of engineering ceramic materials, such as silicon nitride and zirconia. The hybrid ceramic ball bearings have the advantages of longer service life and higher stiffness than conventional steel bearings, and are therefore widely used in fields of automotive industry, aircraft and machine tools [1], [2]. However, there exists great difference in the hardness between rings and balls, thus leading to local spalling on the outer ring.

Spalling is a common type of fault that comes from wear, and happens extensively on the outer ring of hybrid ceramic ball bearing due to the great relative velocity [3]–[7], see Figure 1(a). The size of the spalling is enough to bring effect on the vibration of the bearing, and the circumferential location is usually uncertain, as shown in Figure 1(b).

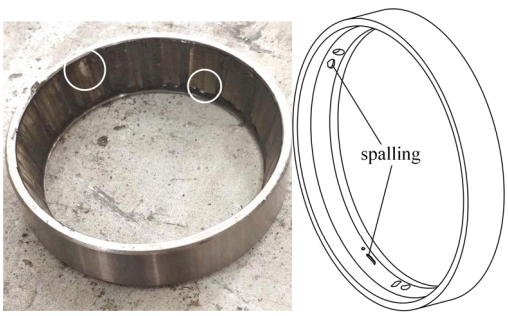

FIGURE 1. Spallings on the outer ring.

Spallings at different locations make different impacts on the contacts between the balls and outer ring, and also have different effects on the bearing vibration and service life. The recognition and localization of the spalling on the outer ring can help monitor the running state of the hybrid ceramic ball bearing, and is of great significance to the health management.

In the past decade, many researchers have focused on the spalling recognition and localization methods, and the main methods include deep learning [8], [9], acoustic

The associate editor coordinating the review of this manuscript and approving it for publication was Huawei Chen.

emission (AE) methods [10], [11] and vibration signal analysis [12]–[14]. Li *et al.* [15] applied the data-driven method, and proposed a deep learning-based method rolling bearing fault diagnosis method. The deep learning method is able to learn the features of the input data, but the recognition accuracy is determined by the training process, and usually takes much time. Sharma and Parey [16] developed a mathematical model of the bearing to predict the AE responses with faults. Wang *et al.* [17] focused on the feature extraction to recognize the feature stages of rolling bearing based on AE technique. Works done by AE techniques have proved that the method is effective at stable working conditions, but the results are less accurate at variable working conditions. Methods based on the vibration signals are the most widely used in the recognition and localization of faults, and the recognition are based on the dynamic modeling [18]–[21]. Chen and Thomas [22] built a bearing model, and proposed signal processing techniques to estimate the spalling size. Luo *et al.* [23] carried out an investigation into the spall defect excitation mechanism, and proposed a model to analyze the contact between the rolling element and the spall area. Kogan *et al.* [24] developed two generic and autonomous algorithms for the estimation of bearing spall width based on the vibration signals. Cui *et al.* [25] built the relationship between the horizontal and vertical vibration signals, and developed a localization law for the spalling on the outer ring based on the horizontal-vertical root mean square.

The recognition method based on the vibration signals is more detailed, and seems to be able to provide the locations of the spalling theoretically. However, the arrangement of sensors is usually limited by the structures, and the recognition is also affected. Sound signals are obtained through non-contact measurement, and are easier accessed and more convenient for accurate localization [26], [27]. Works by Amarnath *et al.* [28] and Lu *et al.* [29] have proved the effectiveness of fault detection based on sound signals, and the relationship between the vibration and sound radiation were also investigated in previous works [30], [31]. A localization method of spalling on the outer ring is quite essential for the status monitoring and health management of the hybrid ceramic ball bearing. In this paper, the dynamic model with a spalling is proposed, and the sound radiation model is established based on the sub-source decomposition method. The sound signals with different spalling locations are obtained though numerical simulation, and the locations of spalling are recognized through the characteristics in the sound signals. Experiments are conducted to verify the accuracy of the localization strategy, and conclusions are drawn at last.

II. GUIDELINES FOR MANUSCRIPT PREPARATION

The contact model of the bearing with the effect of spalling is shown in Figure 2, and the cage is not shown here.

In Figure 2, the positions are described in coordinate system $\{O;\ X,\ Y,\ Z\}$, and ϕ_j shows the azimuth angle of the jth ball. $F_{\mathrm{R}\xi ij}$ and $F_{\mathrm{R}\eta ij}$ show the friction force between the jth ball and the inner ring in plane YOZ and XOZ, and $F_{\mathrm{R}\xi oj}$

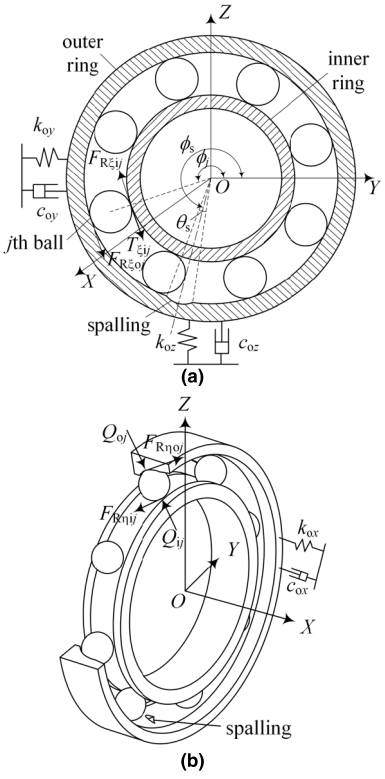

FIGURE 2. Contact model between the elements in (a) YOZ plane and (b) XOZ plane.

and $F_{\mathrm{R}\eta oj}$ show the friction force between the jth ball and the outer ring, respectively. $Q_{\mathrm{i}j}$ is the contact pressure between the inner ring and the jth ball, and $Q_{\mathrm{o}j}$ is the contact pressure between the outer ring and the jth ball. The outer ring is placed in the pedestal, and the inner ring rotates with the shaft. $T_{\xi ij}$ shows the traction force by the inner ring. $k_{\mathrm{o}x}$, $k_{\mathrm{o}y}$ and $k_{\mathrm{o}z}$ are the contact stiffness of the pedestal in OX, OY and OZ directions, and $c_{\mathrm{o}x}$, $c_{\mathrm{o}z}$ and $c_{\mathrm{o}y}$ are the damping coefficients. The spalling is located at the azimuth angle of ϕ_{s}, and the width of the spalling is θ_{s}. Assuming that the outer ring has no angular displacement, and the effects of surface roughness and structural errors are neglected. When no balls are in the spalling area, the dynamic equations of the inner ring can be expressed as

$$F_x + \sum_{j=1}^{N} \left(F_{\mathrm{R}\eta ij}\cos\alpha_{ij} - Q_{\mathrm{i}j}\sin\alpha_{ij}\right) = m_{\mathrm{i}}\ddot{x}_{\mathrm{i}} \tag{1}$$

$$F_y + \sum_{j=1}^{N} \left[\left(Q_{\mathrm{i}j}\cos\alpha_{ij} + F_{\mathrm{R}\eta ij}\sin\alpha_{ij}\right)\cos\phi_j + \left(T_{\xi ij} - F_{\mathrm{R}\xi ij}\right)\sin\phi_j\right] = m_{\mathrm{i}}\ddot{y}_{\mathrm{i}} \tag{2}$$

$$F_z + \sum_{j=1}^{N} \left[\left(Q_{\mathrm{i}j}\cos\alpha_{ij} + F_{\mathrm{R}\eta ij}\sin\alpha_{ij}\right)\sin\phi_j - \left(T_{\xi ij} - F_{\mathrm{R}\xi ij}\right)\cos\phi_j\right] - m_{\mathrm{i}}g = m_{\mathrm{i}}\ddot{z}_{\mathrm{i}} \tag{3}$$

where F_x, F_y and F_z are external loads, and N is the total number of balls. m_{i} is the mass of the inner ring, and α_{ij} is the

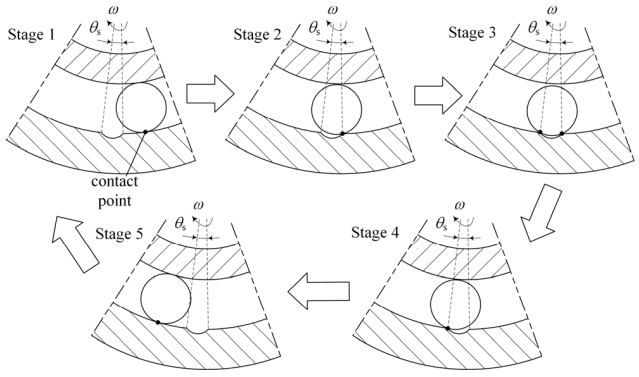

FIGURE 3. The ball passing the spalling area.

contact angle between the inner ring and the jth ball. $\ddot{x}_i$, $\ddot{y}_i$, $\ddot{z}_i$ are accelerations along axes OX, OY and OZ, respectively. For the outer ring, there is

$$\sum_{j=1}^{N}\left(F_{R\eta oj}\cos\alpha_{oj}-Q_{oj}\sin\alpha_{oj}\right)-k_{ox}x_o-c_{ox}\dot{x}_o=m_o\ddot{x}_o \quad (4)$$

$$\sum_{j=1}^{N}\left[\left(F_{R\eta oj}\sin\alpha_{oj}+Q_{oj}\cos\alpha_{oj}\right)\cos\phi_j-F_{R\xi oj}\sin\phi_j\right] - k_{oy}y_o-c_{oy}\dot{y}_o=m_o\ddot{y}_o \quad (5)$$

$$\sum_{j=1}^{N}\left[\left(F_{R\eta oj}\sin\alpha_{oj}+Q_{oj}\cos\alpha_{oj}\right)\sin\phi_j+F_{R\xi oj}\cos\phi_j\right] - m_o g-k_{oz}z_o-c_{oz}\dot{z}_o=m_o\ddot{z}_o \quad (6)$$

where α_{oj} shows the contact angle between the jth ball and the outer ring, and m_o is the mass of the outer ring. x_o, y_o and z_o are displacements of the outer ring along axes OX, OY and OZ, and $\dot{x}_o$, $\dot{y}_o$, $\dot{z}_o$, $\ddot{x}_o$, $\ddot{y}_o$ and $\ddot{z}_o$ are the corresponding velocities and accelerations. Here the shape of the spalling is regarded as a hollow with an arc section, and the ball passes through the spalling area in the way shown in Figure 3. When the location of the spalling is confirmed, the motion of the ball can be divided into five stages:

Stage 1. Before entering the spalling area, with $\phi_j > \phi_s + \theta_s/2$. The contact between the ball and the rings is not affected by the spalling, and the dynamic characteristics of the rings can be obtained through Eqs.(1)-(6).

Stage 2. The ball starts to enter the spalling area, with $\phi_s < \phi_j < \phi_s+\theta_s/2$. The distance between the bearing center to the ball center increases, and the ball is out of contact with the inner ring. For a ball in stage 2, the contact force Q_{ij} can be ignored.

Stage 3. The ball arrives at the limit position at $\phi_j = \phi_s$. Here the radius of the spalling is supposed to be smaller than the ball radius, and the ball cannot reach the bottom of the spalling. When the ball arrives at the position in stage 3, an impact force F_j' is added to the outer ring.

Stage 4. The ball passes the lowest point, and starts to come out of the spalling area. In the angle interval of ϕ_s-$\theta_s/2 < \phi_j < \phi_s + \theta_s/2$, the jth ball is not in contact with the inner ring.

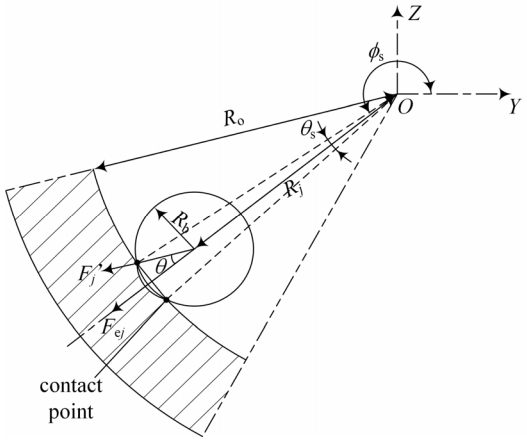

FIGURE 4. Forces acting on the outer ring at the spalling area.

Stage 5. The ball comes out of the spalling, and the ball will run by the circumference until it reaches the spalling again, as in stage 1.

In general, when the ball passes through the spalling area, the forces acting on the inner ring and the outer ring have changed. For the inner ring, the force Q_{ij} no longer exists in the spalling zone, and the number of balls N needs to be revised to (N-1) in the period of ϕ_s-$\theta_s/2 < \phi_j < \phi_s + \theta_s/2$. For the outer ring, the impact force when the ball arrives at the limit position at $\theta_j = \theta_s$ in stage 3 can be shown in Figure 4.

In Figure 4, R_o shows the bore radius of the outer ring, and R_b shows the radius of the ball. F_{ej} is the centrifugal force of the jth ball, and can be expressed as

$$F_{ej} = m_j\omega^2 R_j \quad (7)$$

where m_j shows the mass of the jth ball, and ω is the rotation speed of the bearing. R_j is the rotation radius at the spalling area, and can be expressed as

$$R_j = R_o\cdot\cos\frac{\theta_s}{2}-\sqrt{R_b^2-\left(R_o\cdot\sin\frac{\theta_s}{2}\right)^2} \quad (8)$$

And F_j' is related with F_{ej} as

$$F_j' = F_{ej}\cdot\cos\theta = F_{ej}\cdot\frac{\sqrt{R_b^2-\left(R_o\cdot\sin\frac{\theta_s}{2}\right)}}{R_b} \quad (9)$$

As a result, when the impact forces of the balls passing through the spalling area are taken into consideration, changes occur to the dynamic equations of the outer ring as (10) and (11), as shown at the bottom of the next page. According to the sub-source decomposition method derived in Ref. [31], the sound radiation of the hybrid ceramic ball bearing can be regarded as the superposition result of the sound radiation from the inner ring, balls, the cage and the outer ring. It has been proved in previous works [30], [31] that the sound radiation from the rings are dominant in the overall sound radiation, and determines the main frequency components. As a result, the superposition result of the inner

ring and outer ring sound radiation is investigated, and the sound radiation can be expressed as

$$p(x) = \sum_{s} p_s(x) = \mathbf{a}_i^T \cdot \mathbf{p}_i + \mathbf{b}_i^T \cdot \mathbf{v}_{ni} + \mathbf{a}_o^T \cdot \mathbf{p}_o + \mathbf{b}_o^T \cdot \mathbf{v}_{no} \quad (12)$$

where $p(x)$ is the sound pressure at the field point x, and here s = i, o denotes the sound source. $\mathbf{p}$ and $\mathbf{v}_n$ are the surface sound pressure and the normal velocity vectors, and $\mathbf{a}$ and $\mathbf{b}$ are coefficient matrices. The surface sound pressure is related with the vibration as

$$\mathbf{A} \cdot \mathbf{p}_s = \mathbf{B} \cdot \mathbf{v}_{ns} \quad (13)$$

where $\mathbf{A}$ and $\mathbf{B}$ are impact coefficient matrices related with surface condition and wave numbers. The sound pressure level at the field point x can be derived from the sound pressure as

$$S(x) = 20 \lg \frac{p(x)}{p_{ref}} \quad (14)$$

where p_{ref} = 2e-5Pa is the reference sound pressure, and the sound pressure level at the reference sound pressure is 0dB. Then the sound pressure levels of the hybrid ceramic ball bearing can be obtained through Eqs.(12)-(14), and the distribution of sound pressure levels with different spalling locations can be investigated. For detailed derivation one can refer to Ref. [31].

III. NUMERICAL SIMULATION

Here a comparative study on healthy bearing and bearing with outer ring spalling is conducted. According to previous research, the characteristic frequency f_o appears when the spalling is taken into consideration in the model, where

$$f_o = N \cdot f_r \cdot \frac{1 - \frac{2R_b}{d_m} \cdot \cos \alpha_n}{2} \quad (15)$$

where f_r is the rotation frequency, d_m is the pitch diameter of the bearing, and α_n is the nominal contact angle of the bearing. Assuming that the shape centers of the components match with the mass centroids, and the bearing works with perfect lubrication. The impacts of the shape errors and the surface roughness are neglected, and no defects on the bearing is taken into consideration for the healthy bearing case. The bearing has the same parameters with 7003C, and the major parameters of the bearing are shown in Table1.

The bearing has a rotation speed of 15000rpm, and the effect of speed fluctuation is ignored. The axial preload is set as 200N, and the radial load including the mass of the shaft, is 100N. The bearing can be considered as a sound source with the shape of cylinder, and the sound radiation is

TABLE 1. Major parameters of the hybrid ceramic ball bearing.

Item	Value
Outer ring outside diameter(mm)	35
Outer ring inside diameter(mm)	29.2
Bearing width(mm)	10
Cage outside diameter(mm)	26.5
Cage bore diameter(mm)	23.8
Pocket diameter(mm)	5
Cage width(mm)	8.8
Inner ring outside diameter(mm)	23
Inner ring bore diameter(mm)	17
Ball number	15
Ball diameter(mm)	4.5
Nominal contact angle(degree)	15

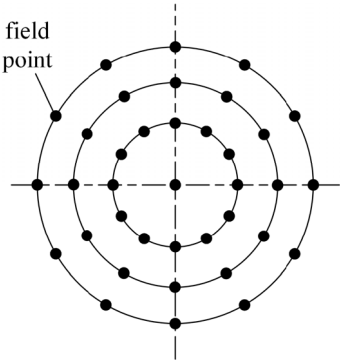

FIGURE 5. Arrangement of field points.

proposed to be collected by a circular sensor array. Then the sound radiation results are expressed as $S = S(\psi)$, where ψ is the azimuth of the field point. The field points are arranged on concentric circles, with one point at the center, as shown in Figure 5.

The dynamic characteristics of the healthy hybrid ceramic ball bearing are obtained through Eqs.(1)-(6), and the sound radiation is acquired through Eqs.(12)-(14). On each circle there are 30 field points evenly distributed with an angular interval of 6 degrees, and the time-domain Real Mean Square(RMS) values at the field points arranged on the circles are analyzed. Here ψ is used to represent the azimuth of the sound radiation. For the field points, the 12 o'clock direction is set as $\psi = 0°$, and the angles have a clockwise arrangement. Here the plane for field points is set perpendicular to the axis of the bearing, and the axial distance from the bearing to the field point plane is 100mm. The diameters of the concentric circles are 60mm, 260mm and 460mm. For the center point, the Fast Fourier Transform(FFT) is applied to

$$\sum_{j=1}^{N} \left[\left(F_{R\eta oj} \sin \alpha_{oj} + Q_{oj} \cos \alpha_{oj} \right) \cos \phi_j - F_{R\xi oj} \sin \phi_j + F_j' \cos(\phi_s - \theta) \right] - k_{oy} y_o - c_{oy} \dot{y}_o = m_o \ddot{y}_o \quad (10)$$

$$\sum_{j=1}^{N} \left[\left(F_{R\eta oj} \sin \alpha_{oj} + Q_{oj} \cos \alpha_{oj} \right) \sin \phi_j + F_{R\xi oj} \cos \phi_j + F_j' \sin(\phi_s - \theta) \right] - m_o g - k_{oz} z_o - c_{oz} \dot{z}_o = m_o \ddot{z}_o \quad (11)$$

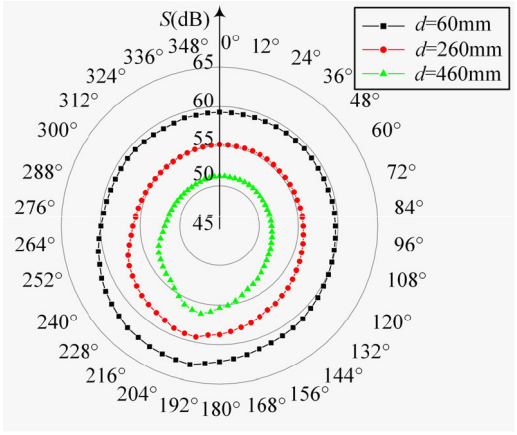

(a) Circumferential distributions on the concentric circles

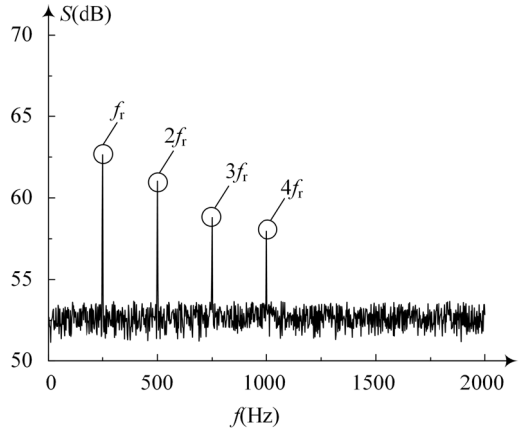

(b) Frequency-domain results at the center point

FIGURE 6. Simulation results of a healthy bearing.

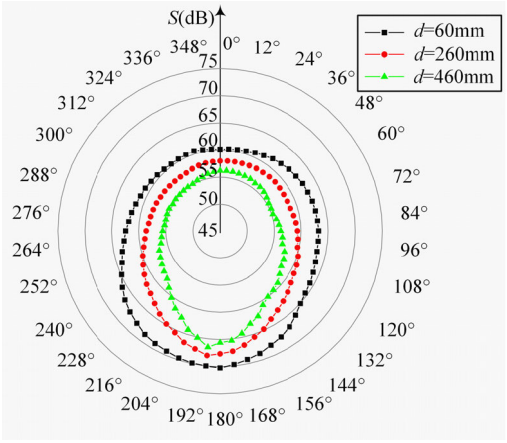

(a) Circumferential distributions on the concentric circles

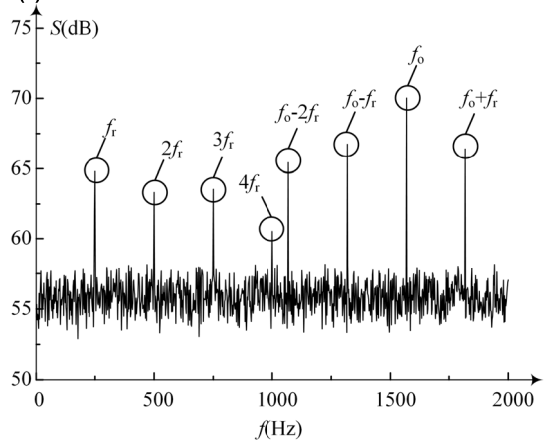

(b) Frequency-domain results at the center point

FIGURE 7. Simulation results with a spalling.

acquire the result in frequency domain. The upper limit for the analysis is 2000Hz, and the frequency step is 2Hz. The results are shown in Figure 6.

It can be seen in Figure 6 that the distributions of sound radiation tend to be slightly uneven on the circles, and the attenuation of the sound pressure levels varies in different directions. In frequency domain, there exists four main peaks in the frequency result of a healthy bearing. The peaks are f_r, $2f_r$, $3f_r$ and $4f_r$, where f_r is 250Hz here. Then a spalling is considered in the model for the comparative study. The spalling is located at $\phi_s = 270°$ with a size of $\theta_s = 4°$, and the spalling is deep enough to keep the balls from touching the bottom. Then the dynamic characteristics of the inner ring and the outer ring need to be fixed through Eqs(7)-(11). The other parameters remain the same, and the sound radiation results are shown in Figure 7.

As shown in Figure 7, the sound pressure level increases when there is a spalling, and there also appears more peaks related with f_o. Compared with the results in Figure 6, the distributions of the sound radiation in Figure 7 are larger in circumferential differences. The peak angle of the sound radiation, which refers to the azimuth of the maximum sound pressure level, has a shift from $\psi = 192°$ to $\psi = 180°$. It is clear that the results in frequency domain are more complex, and the frequency components related with f_o take the dominant positions in the vibration of the bearing. The frequency components related with f_r still exist in the result, but the amplitudes are obviously lower. The spalling brings changes to the dynamic model, and thus leading to the change of sound radiation. Therefore, it can be concluded that the spalling makes great impact on the sound radiation of the hybrid ceramic ball bearing, and the location of the spalling is included in the distribution of the sound radiation.

IV. CASE STUDIES

It has been proved that the appearance of the spalling leads to changes in the distribution of sound radiation, and the changes are related with the location of the spalling. Here the outer ring is divided into three parts, the unloaded zone, the forward loaded zone and the backward loaded zone. The unloaded zone refers to the upper 2/3 of the circumference, and the spalling is located in the unloaded zone when $0° < \phi_s < 210°$ and $330° < \phi_s < 360°$. The forward loaded zone refers to the part of the loaded zone in the side of rotation direction, with the angle of $210° < \phi_s < 270°$, and the backward loaded zone refers to the other part of the loaded

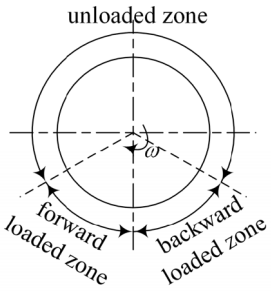

FIGURE 8. Division of the sections.

zone with the angle of $270° < \phi_s < 330°$. The division of each section is shown in Figure 8.

A. SPALLING IN THE UNLOADED ZONE

First the case that the spalling occurs in the unloaded zone is studied. Two situations when $\phi_s = 30°$ and $\phi_s = 150°$ are analyzed, and the sound radiations are calculated respectively. The size of the spalling is $\theta_s = 4°$. The working condition parameters are the same as the numerical simulation, and the other sources of interference are ignored. The arrangement of the field points is the same as in Figure 5, and there are 60 points on each circle with an angular interval of 6°. The diameters of the field point circles are 60mm, 260mm and 460mm, and the time-domain RMS results of the sound radiation are shown in Figure 9.

Compared with the results of a healthy bearing in Figure 6(a), the results have obvious peaks at $\psi = 60°$ and 300°, and the differences are not obvious in other angles. The angles of $\psi = 60°$ and 300° correspond to the azimuths of $\phi_s = 30°$ and 150° respectively, indicating that the spalling in the unloaded zone has a significant impact on the sound radiation, especially at the corresponding angle. However, the spalling is hardly recognized from the near field sound signals such as $d = 60$mm, because the near-field sound pressure levels in the unloaded zone are smaller than those in the loaded zone. In the unloaded zone, the load from the inner ring is not carried by the balls, and the sound radiation mainly comes from the friction between the balls and the outer ring. While in the loaded zone, where the load is carried by the balls, the balls are in contact with the inner ring and the outer ring simultaneously. Therefore, the circumferential sound radiation in the near field is not enough. It can be seen in Figure 9 that the sound pressure level at the spalling azimuth has less attenuation than at the nearby angles with the increase of d, and shows a clear directivity. When the attenuation in radial direction is considered, an indicator can be expressed as

$$\Delta S(\psi) = S(\psi, d_{\min}) - S(\psi, d_{\max}) \tag{16}$$

where $d_{\min}$ and $d_{\max}$ are the minimum and maximum field points diameters, and here are 60mm and 460mm. The circumferential attenuation when $\phi_s = 30°$ and 150° are shown in Figure 10.

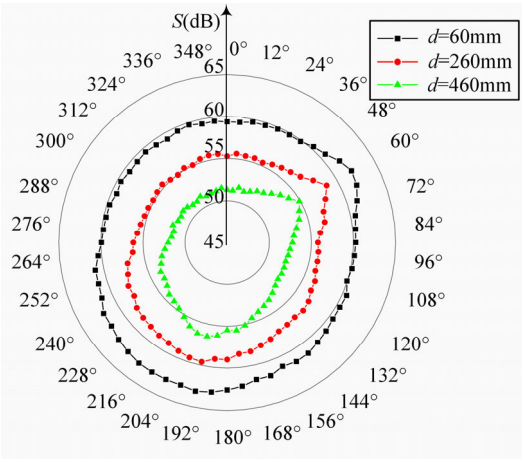

(a) Results when ϕ_s=30°

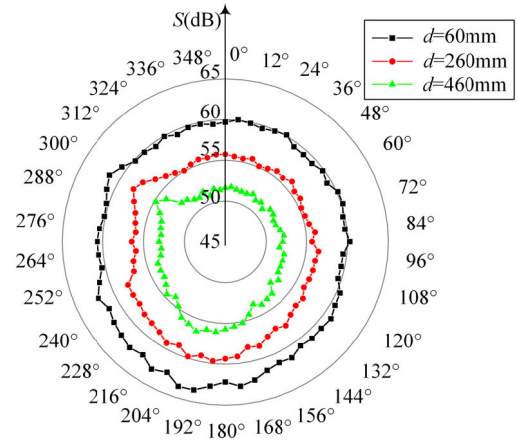

(b) Results when ϕ_s=150°

FIGURE 9. Sound radiation results when the spalling is in the unloaded zone.

As shown in Figure 10, the attenuation values are relatively small at the spalling azimuths, but are not global minimums for recognition. The localization of the spalling is not accurate enough using the time-domain sound pressure levels, and more information in frequency domain is needed. It can be seen from Figure 9 and Figure 10 that the sound pressure levels at around 180° are larger than those at the spalling angles, and here the frequency results at the spalling angles and $\psi = 180°$ with $d = 60$mm are analyzed. The results are shown in Figure 11.

It can be seen in Figure 11 that the frequency components are not the same at different azimuths. At the spalling azimuths in Figure 11(a) and (c), the frequencies related with f_o have greater amplitudes, while at the azimuths of 180° in Figure 11(b) and (d), the frequency components related with rotation speed take the dominance. When the amplitude of f_o is selected as an indicator, then the trends of $S(f_o)$ with ψ on the circles of $d = 60$mm are shown in Figure 12.

As shown in Figure 12, the amplitudes of f_o arrive at the peak values at the spalling azimuths. However, the differences between the values of the spalling azimuths and the

TABLE 2. Localization effects using different indicators when $\phi_s = 30°$ and 150°.

Indicators	Actual azimuth (degree)	Recognized azimuth (degree)	Error (degree)	Actual azimuth (degree)	Recognized azimuth (degree)	Error (degree)
$S(\psi)$	60	192	132	300	198	102
$\Delta S(\psi)$	60	168	108	300	180	120
$S(f_o, \psi)$	60	60	0	300	300	0
$\Delta S(f_o, \psi)$	60	60	0	300	300	0

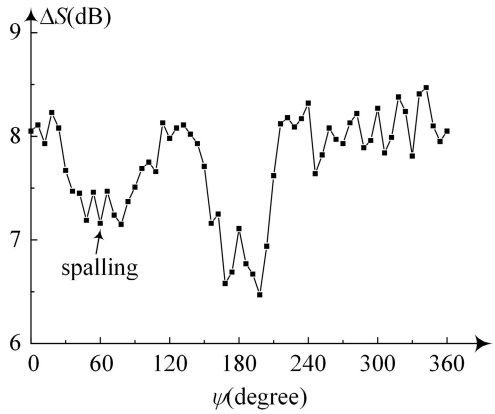

FIGURE 10. Circumferential attenuation with different spalling locations.

adjacent angles are less than 1 dB, which is insufficient for the accurate recognition. As a result, an indicator with more obvious distinction is needed as a supplement for the accurate localization. When the radial attenuation of $S(f_o)$ is considered, the indicator can be expressed as

$$\Delta S\left(f_o, \psi\right) = S\left(f_o, \psi, d_{\min}\right) - S\left(f_o, \psi, d_{\max}\right) \qquad (17)$$

where $\Delta S(f_o, \psi)$ shows the radial attenuation of the amplitude of f_o at the azimuth of ψ. When the diameter of field points changes from 60mm to 460mm, the radial attenuation with $\phi_s = 30°$ and $\phi_s = 150°$ are respectively shown in Figure 13(a) and (b).

As shown in Figure 13, the radial attenuation $\Delta S(f_o)$ has an obvious decrease at the spalling azimuth. The radial attenuation of amplitude of f_o is not only a remarkable local minimum at the spalling azimuth, but also a global minimum in the circumference. It can be inferred that the characteristic frequencies of the spalling still exist in the far-field sound radiation, and the attenuation of the sound radiation is not obvious in the direction of the spalling. Then the location of the spalling can be clearly recognized from the result, and is of good accuracy.

The sound radiation results of the hybrid ceramic ball bearing with spalling in the unloaded zone are displayed in Figure 9-Figure 13, and four indicators $S(\psi)$, $\Delta S(\psi)$, $S(f_o, \psi)$ and $\Delta S(f_o, \psi)$ have been used in the spalling localization. In the localization strategies, the maximums of $S(\psi)$ and $S(f_o, \psi)$ are used to recognize the spalling location as well as the minimum values of $\Delta S(\psi)$ and $\Delta S(f_o, \psi)$. Then the effects of the localization indicators when $\phi_s = 30°$ and 150° are shown in Table 2.

It is clear that for the case that the spalling is located in the unloaded area, the indicators $S(f_o, \psi)$ and $\Delta S(f_o, \psi)$ are more suitable for the spalling localization.

B. SPALLING IN THE FORWARD LOADED ZONE

When a spalling is located in the loaded zone, changes occur to the contact between the loaded balls and the rings. First the case that the spalling is located in the forward loaded zone is discussed. Assuming that there is a spalling located at $\phi_s = 240°$, which correspond to $\psi = 210°$, and the size of the spalling is 4°. The working parameters and field points arrangement are the same as Section 4.1, and the circumferential distribution of the sound radiation is shown in Figure 14.

According to the results of a healthy bearing in Figure 7(a), the peak value for the sound radiation appears at around 192°. When the spalling is located nearby, there will be only one peak in the superposition result, and the peak has a shift towards the spalling direction. As a result, there is only one obvious peak in the circumference in Figure 14, which is different from the case of the unloaded zone. The directivity of the sound radiation curve turns clearer with the increase of field point diameter, and the radial attenuation of the sound radiation is shown in Figure 15.

As shown in Figure 15, the radial attenuation of the sound radiation has an obvious decrease between 186° and 210°, and the minimum value appears at 204°. The localization error is acceptable, however, the difference between 186° and 210° is very small, and the localization result is easily affected when the working condition changes.

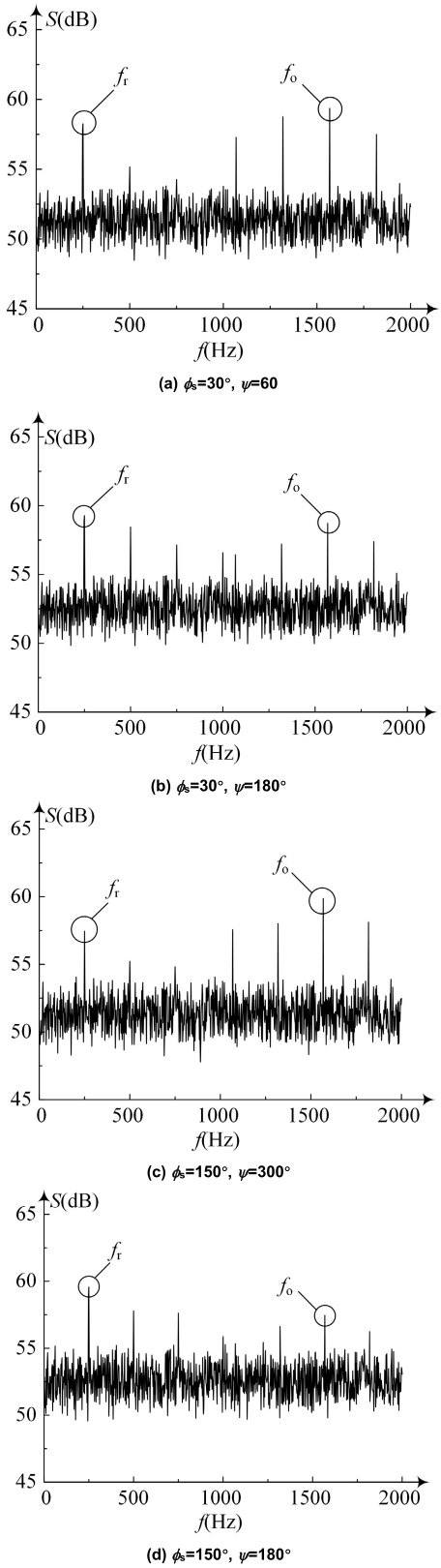

FIGURE 11. Frequency results at different points.

Then the results in frequency domain is obtained through FFT, and the results of $S(f_o)$ and $\Delta S(f_o)$ are shown in Figure 16.

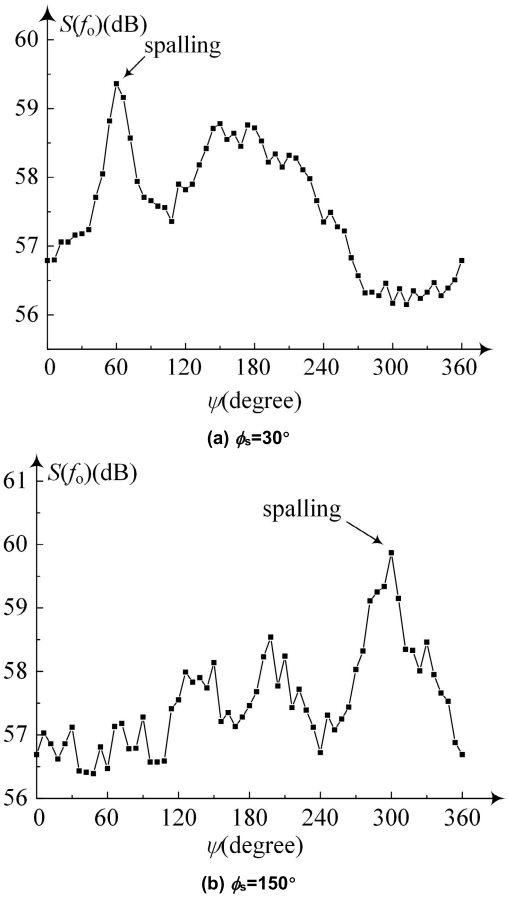

FIGURE 12. Amplitudes of $S(f_o)$ at different azimuths.

TABLE 3. Localization effects using different indicators when $\phi_s = 240°$.

Indicators	Actual azimuth (degree)	Recognized azimuth (degree)	Error (degree)
$S(\psi)$	210	198	12
$\Delta S(\psi)$	210	204	6
$S(f_o, \psi)$	210	204	6
$\Delta S(f_o, \psi)$	210	210	0

In Figure 16(a), the frequency component of f_o stays at high levels from 180° to 216°, indicating that the sound radiation is greatly affected by the spalling, and the f_o component has a large radiation range in the near field. In that case, the differences among the azimuths close to the spalling are small, thus bringing difficulty in the accurate localization of the spalling. However, the sound radiation has directivity, and the attenuation of the frequency components are different in the radial direction. Therefore, as the field point diameter increases, the amplitude of f_o has less decline in the direction of the spalling, and then the spalling azimuth can be clearly recognized through the radial attenuation of $S(f_o)$, as shown in Figure 16(b). The effects of the indicators when $\phi_s = 240°$ are shown in Table 3.

The errors of the localization using the indicators in Table 3 reach up to 12°, and the localization seem to be passable by all the four indicators. However, the small errors are due to the fact that the spalling is located in the

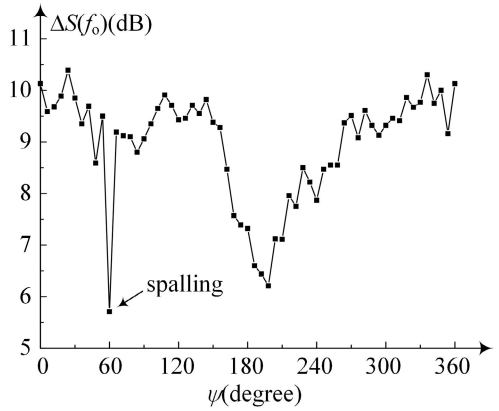

(a) ϕ_s=30°

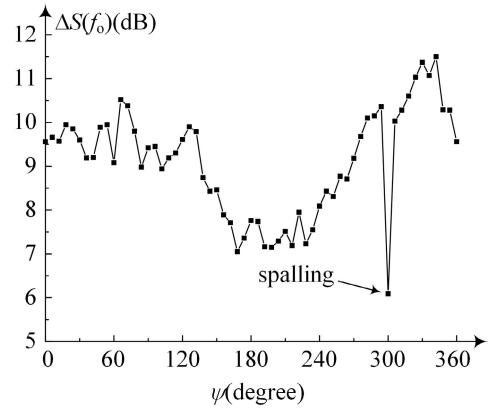

(b) ϕ_s=150°

FIGURE 13. Radial attenuation of $S(f_o)$ at different azimuths.

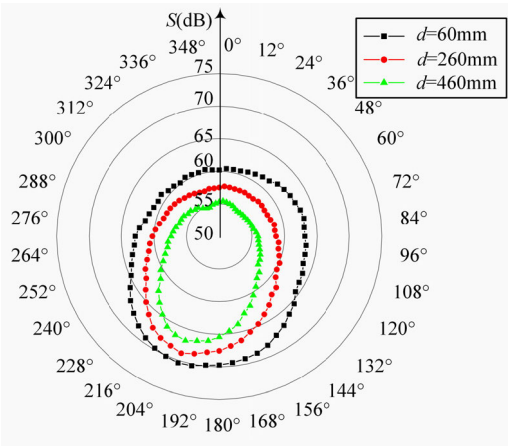

FIGURE 14. Circumferential distribution of the sound radiation when $\phi_s = 240°$.

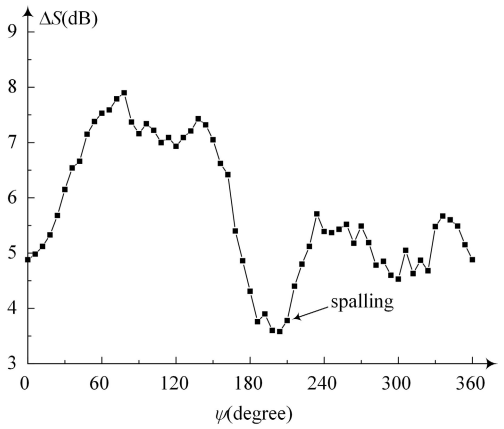

FIGURE 15. Radial attenuation when $\phi_s = 240°$.

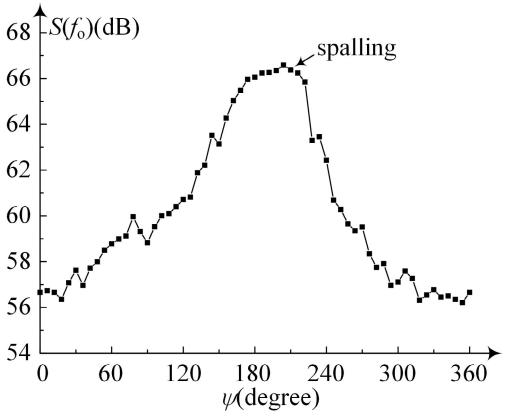

(a) Amplitude of f_o

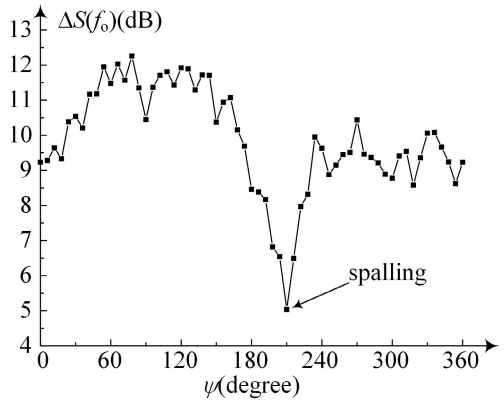

(b) Amplitude of the attenuation of f_o

FIGURE 16. Trends of $S(f_o)$ and $\Delta S(f_o)$ in the circumference when $\phi_s = 240°$.

forward loaded zone, and is not far from the original peak angle of the sound radiation. In this case, the original peak angle of the sound radiation is $\psi = 192°$, and the spalling is located at $\psi = 210°$. The angle difference is only 18°, and the peak value of the sound radiation with spalling is between the two angles, which brings difficulty in the accurate localization of the spalling. When $\Delta S(\psi)$ or $S(f_o, \psi)$ is selected as the indicator, the minimum difference between the adjacent values is below 0.15 dB, and the localization result is not able to be clearly recognized. When $\Delta S(f_o, \psi)$ is applied as the indicator, the minimum difference between the adjacent values is over 1.4 dB. Therefore, the indicator is more suitable, and the localization result is more credible.

C. SPALLING IN THE BACKWARD LOADED ZONE

At last the case of backward loaded zone is considered, and the spalling is located at $\phi_s = 300°$ with $\theta_s = 4°$.

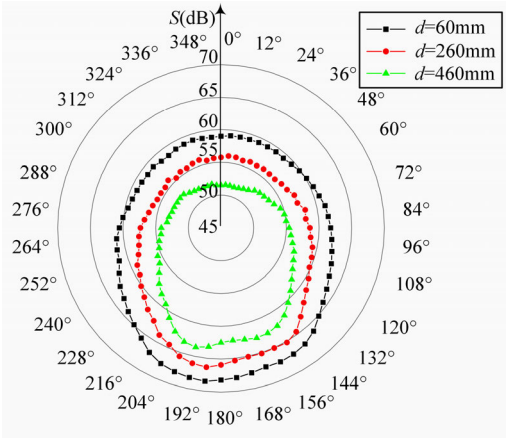

FIGURE 17. Circumferential distribution of the sound radiation when $\phi_s = 300°$.

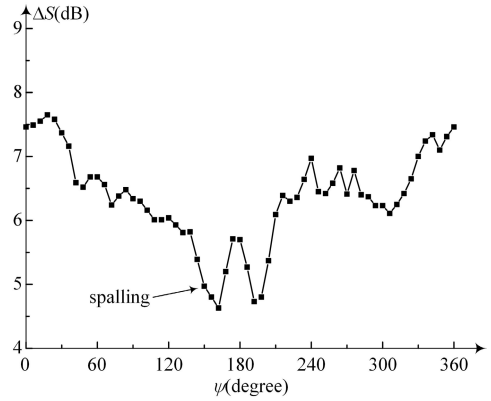

FIGURE 18. Radial attenuation when $\phi_s = 300°$.

The corresponding azimuth for field points is $\psi = 150°$, and the field points are arranged in the same way as the former sections. The working condition parameters stay unchanged, and the other interference brought by the shape errors are ignored. The circumferential distribution of the time-domain sound pressure levels at $d = 60$mm is shown in Figure 17.

In this case, the spalling is also located in the loaded zone, but the interval between the spalling azimuth and the original peak angle is larger. According to the model proposed above, impact sound radiations are produced when the balls pass the spalling, and the sound pressure levels in directions between the spalling and the original peak angle are obviously affected. As a result, the near field sound radiation is at high levels in a wide range between the spalling azimuth and the original peak angle, as displayed in Figure 17. Compared with the results in Figure 9 and Figure 14, there is no obvious peak in the circumferential distribution. When the diameter of the field points increases, two local maximum values appear at around 150° and 186°, and the sound pressure levels at the azimuths between the two angles have greater declines. The radial attenuation of the sound radiation is shown in Figure18.

As shown in Figure 18, the radial attenuation has two local minimums at 162° and 192°. The attenuation at the spalling

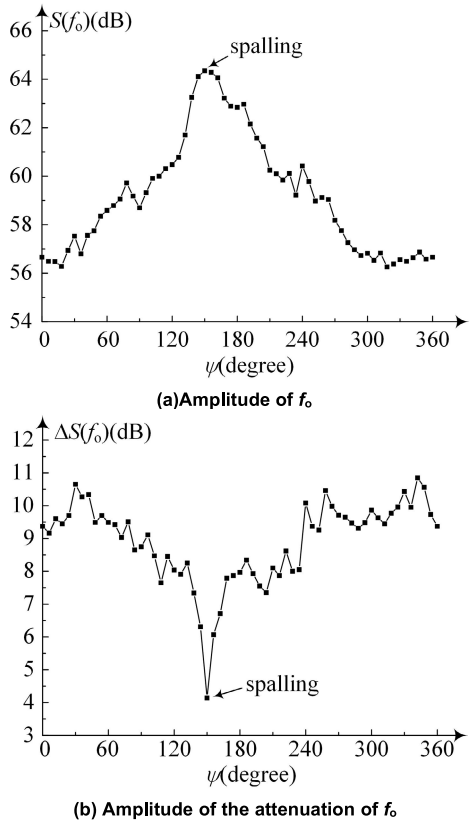

FIGURE 19. Trends of $S(f_o)$ and $\Delta S(f_o)$ in the circumference when $\phi_s = 240°$.

TABLE 4. Localization effects using different indicators when $\phi_s = 300°$.

Indicators	Actual azimuth (degree)	Recognized azimuth (degree)	Error (degree)
$S(\psi)$	150	186	36
$\Delta S(\psi)$	150	162	12
$S(f_o, \psi)$	150	150	0
$\Delta S(f_o, \psi)$	150	150	0

azimuth is among the smaller values, but is not able to be recognized from the curve. The frequency domain information is needed to localize the spalling, and the circumferential values of $S(f_o)$ and $\Delta S(f_o)$ are shown in Figure 19.

According to the recognition principles proposed above, the localization results by $S(f_o)$ and $\Delta S(f_o)$ are 150°, and both results match well with the model. It is implied that the frequency component of f_o is more concentrated in the sound radiation near the spalling, and the position of the spalling can be more accurately localized through the frequency results. The effects of the indicators when $\phi_s = 300°$ are shown in Table 4.

It is shown in Table 4 that the localization strategies by indicators of $S(f_o)$ and $\Delta S(f_o)$ can meet the requirement, however, the recognition of the results are of different clarity. The localization result in Figure 19(a) is recognized in a difference of less than 0.1 dB, while the amplitude of the localization result in Figure 19(b) has an advantage of about 2 dB.

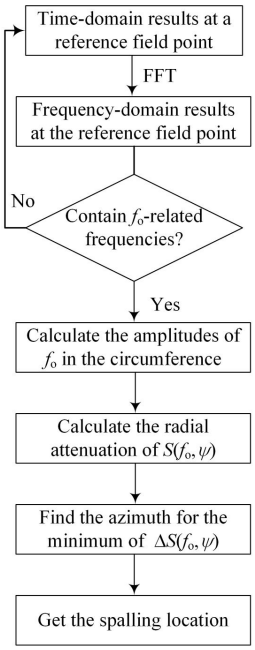

FIGURE 20. Localization strategy with the indicator of $\Delta S(f_o)$.

FIGURE 21. Photos of the experimental devices.

Therefore, the recognition by $\Delta S(f_o)$ is clearer. In general, it can be concluded from the above cases that the frequency results are essential for the localization of the spalling, and the radial attenuation of the characteristic frequency of the spalling, $\Delta S(f_o)$, is more suitable for the localization. According to the investigations conducted above, the localization strategy of the spalling can be expressed as in Figure 20.

As shown in Figure 20, a series of measuring points with an appropriate circumferential and radial distribution are needed for the localization of the spalling, and a reference point is needed to check if there is a spalling in the bearing. When a spalling is detected from the frequency results at the reference point, the frequency-domain results in the circumferences are obtained through FFT. Then the radial attenuation of the amplitudes of f_o from the smallest circle to the largest circle are calculated, and the minimum azimuth for $\Delta S(f_o)$ can be acquired as the localization result of the spalling.

V. EXPERIMENTAL INVESTIGATIONS

An experimental investigation is designed here for the verification of the localization method, and the experiment is conducted on the ceramic motorized spindle test rig. The hybrid ceramic ball bearings are installed at both ends of the spindle, and the type of the bearing is 7003C. To simulate the fault of spalling, a through hole with a diameter of 1mm is processed on the outer ring. In the proposed model in Figure 3 and 4, the balls pass the spalling area without touching the bottom of the spalling, and the same situation happens in the experiment when a through hole is made on the outer ring. The bearing at the front end of the spindle is a fault bearing with a outer ring spalling at $\phi_s = 270°$, and the bearing at the rear end is a healthy bearing. The rotation speed of the bearing system can reach up to 60000 rpm, and can be controlled manually, as shown in Figure 21.

The type of the acoustic sensors in Figure 21 is BSWA MPA416, and the sensitivities of the sensors vary from 48.5 mV Pa^{-1} to 50 mV Pa^{-1}. The data collector applied is PAK MK II-SC42, and the sampling frequency is set as 5000Hz. The measuring points are arranged 100mm from the front bearing, and a microphone array is set to guarantee the positions of the acoustic sensors. The microphone array can rotate around the center, and get the circumferential distribution of the sound radiation. The rotation speed of the bearing is set as 15000rpm, and the axial preload and radial load are 200N and 100N, respectively. The ambient temperature is 25 centigrade, and the background noise is below 40dB. The circumferential distribution of the experimental sound radiation results are shown in Figure 22(a). Then the frequency result at the center point is obtained through FFT, as shown in Figure 22(b). After that, the amplitudes of f_o in the circumferences of $d = 60$mm, 260mm and 460mm are counted respectively, and the trend of $\Delta S(f_o)$ is shown in Figure 22(c).

It can be seen from Figure 22(a) that the differences between the sound pressure levels between azimuths of 180° and 204° are not so obvious, and it is hard for the recognition or localization of the spalling from the circumferential distribution of the sound pressure levels in the near field. Compared with the results in Figure 7(a), the results in Figure 22(a) are less regular, and the errors between the

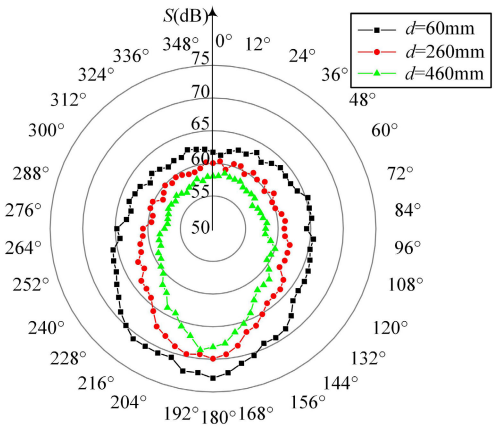

(a) Results of the circumferential distribution

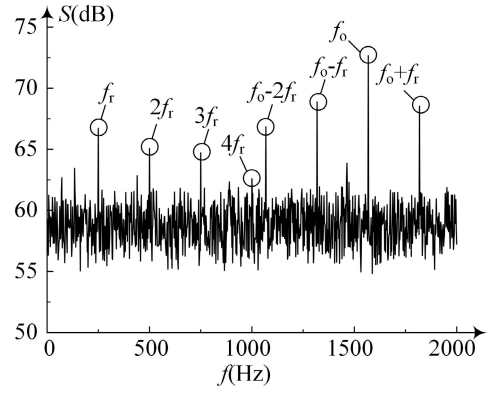

(b) Frequency-domain results at the center point

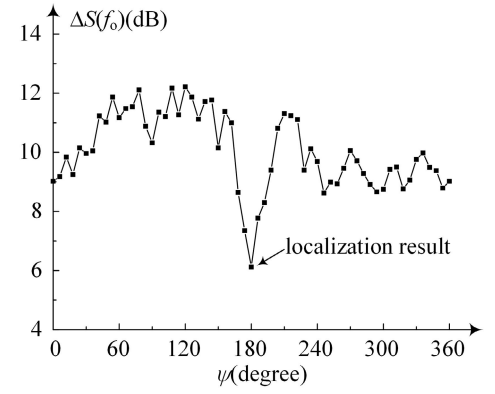

(c) Localization by the indicator of $\Delta S(f_o)$

FIGURE 22. Experimental results and the spalling localization.

calculated and experimental results are acceptable. The errors come from the interference of the sound radiation from the other bearing and the motor, and are not obvious compared with the sound radiation from the bearing with spalling. The frequency- domain result in Figure 22(b) has shown that there are not only rotation speed-related frequency components in the sound radiation at the center, but also the frequencies related with the spalling. The frequency components are similar as Figure 7(b), indicating that the spalling makes great contribution to the overall sound radiation. When the radial attenuation of the amplitudes of f_o is obtained, it can be seen clearly that $\Delta S(f_o)$ has an obvious global minimum at $\psi = 180°$, which is in correspondence to the spalling location of $\phi_s = 270°$. The recognition of the result is quite clear, and the localization result is proved to be in consistence with the actual position of the spalling.

It can be indicated from the cases above that the location of the spalling is hardly seen from the sound pressure levels in the circumference, and the frequency domain information is crucial. Good results are achieved when the amplitude of f_o is set as the indicator, however, the differences between adjacent values are so small that the results are not clearly recognized. The amplitude of $\Delta S(f_o)$ shows the minimum value at the spalling location, and the indicator of $\Delta S(f_o)$ is of high accuracy for the localization of the spalling on the outer ring. The accuracy depends on the number and angular intervals of the sensors, and the localization comes with good effect when the number of measuring points arrives at 60 in a circumference, as shown in the simulations and experiment.

VI. CONCLUSION

The localization methods for the spalling on the outer ring of a hybrid ceramic ball bearing are discussed in this paper, and the characteristics in the sound radiation are investigated based on the dynamic model. It is found that the spalling makes great impact on the circumferential sound pressure levels of the hybrid ceramic ball bearing, and the frequency components also change as the spalling occurs. When there is a spalling on the outer ring, some extra frequency components related with the spalling raise in the frequency results. The frequency components are not fully reflected in the time-domain RMS results, and therefore it is of poor accuracy to localize the spalling through the circumferential distribution of the sound pressure levels. The characteristic frequency of the spalling, f_o, is found to make great contribution to the sound radiation near the spalling. It is found that the radial attenuation of the amplitude of f_o, $\Delta S(f_o)$, varies in different angles, and arrives at the global minimum at the spalling azimuth. The localization results with the indicator of $\Delta S(f_o)$ match well with the model, and the localization strategy is proved of high accuracy through the experiment. This study provides a new method for the accurate localization of the spalling on the outer ring, and is of great significance for the status monitoring and fault diagnosis of hybrid ceramic ball bearings.

REFERENCES

[1] A. Gabelli and G. E. Morales-Espeje, "A model for hybrid bearing life with surface and subsurface survival," *Wear*, vols. 422–423, pp. 223–234, Mar. 2019.
[2] J. Deutsch, M. He, and D. He, "Remaining useful life prediction of hybrid ceramic bearings using an integrated deep learning and particle filter approach," *Appl. Sci.*, vol. 7, no. 7, pp. 649–665, 2017.
[3] P. Gupta and M. K. Pradhan, "Fault detection analysis in rolling element bearing: A review," *Mater. Today, Proc.*, vol. 4, no. 2, pp. 2085–2094, 2017.
[4] J. Liu, Z. Xu, L. Zhou, W. Yu, and Y. Shao, "A statistical feature investigation of the spalling propagation assessment for a ball bearing," *Mechanism Mach. Theory*, vol. 131, pp. 336–350, Jan. 2019.
[5] H. Alian, S. Konforty, R. Klein, M. Tur, J. Bortman, and U. Ben-Simon, "Bearing fault detection and fault size estimation using fiber-optic sensors," *Mech. Syst. Signal Process.*, vol. 120, pp. 392–407, Apr. 2019.

[6] S. Singh, C. Q. Howard, U. G. Köpke, and C. H. Hansen, "Analytical validation of an explicit finite element model of a rolling element bearing with a localised line spall," *J. Sound. Vib.*, vol. 416, pp. 94–110, Mar. 2018.

[7] S. Zhao, L. Liang, G. Xu, J. Wang, and W. Zhang, "Quantitative diagnosis of a spall-like fault of a rolling element bearing by empirical mode decomposition and the approximate entropy method," *Mech. Syst. Signal Process.*, vol. 40, no. 1, pp. 154–177, Oct. 2013.

[8] S. S. Udmale, S. K. Singh, and S. G. Bhirud, "A bearing data analysis based on kurtogram and deep learning sequence models," *Measurement*, vol. 145, pp. 665–677, Oct. 2019.

[9] L. Han, C. C. Yu, Y. Qin, S. Cui, and C. Liu, "Fault diagnosis of rolling bearings in rail train based on exponential smoothing predictive segmentation and improved ensemble learning algorithm," *Appl. Sci.*, vol. 9, no. 15, pp. 3143–3160, Aug. 2019.

[10] M. Kang, J. Kim, and J.-M. Kim, "An FPGA-based multicore system for real-time bearing fault diagnosis using ultrasampling rate AE signals," *IEEE Trans. Ind. Electron.*, vol. 62, no. 4, pp. 2319–2329, Apr. 2014.

[11] B. Kilundu, X. Chiementin, J. Duez, and D. Mba, "Cyclostationarity of Acoustic Emissions (AE) for monitoring bearing defects," *Mech. Syst. Signal Process.*, vol. 25, no. 6, pp. 2061–2072, Aug. 2011.

[12] P. Gao, L. Hou, Y. Chen, and R. Yang, "Local defect modelling and nonlinear dynamic analysis for the inter-shaft bearing in a dual-rotor system," *Appl. Math. Model.*, vol. 68, pp. 29–47, Apr. 2019.

[13] H. Ma and Z. Feng, "Planet bearing fault diagnosis using multipoint optimal minimum entropy deconvolution adjusted," *J. Sound Vibrat.*, vol. 449, pp. 235–273, Jun. 2019.

[14] Y. Liu, Y. Zhu, F. Wang, J. Hong, and K. Yan, "A novel method to model effects of natural defect on roller bearing," *Tribol. Int.*, vol. 122, pp. 169–178, Jun. 2018.

[15] X. Li, W. Zhang, and Q. Ding, "Understanding and improving deep learning-based rolling bearing fault diagnosis with attention mechanism," *Signal Process.*, vol. 161, pp. 136–154, Aug. 2019.

[16] R. B. Sharma and A. Parey, "Modelling of acoustic emission generated in rolling element bearing," *Appl. Acoust.*, vol. 144, pp. 96–112, Jan. 2019.

[17] Z. Wang, X. Wu, Y. Cao, J. Xie, and X. Liu, "Research on feature extraction algorithm of rolling bearing fatigue evolution stage based on acoustic emission," *Mech. Syst. Signal Process.*, vol. 113, pp. 271–284, Dec. 2018.

[18] H. Ma, H. Li, H. Niu, B. Wen, and X. Zhao, "Effects of eccentric phase difference between two discs on oil-film instability in a rotor–bearing system," *Mech. Syst. Signal Process.*, vol. 41, pp. 526–545, Dec. 2013.

[19] A.-B. Ming, W. Zhang, Z.-Y. Qin, and F.-L. Chu, "Dual-impulse response model for the acoustic emission produced by a spall and the size evaluation in rolling element bearings," *IEEE Trans. Ind. Electron.*, vol. 62, no. 10, pp. 6606–6615, Oct. 2015.

[20] Y. Qin, F. Cao, Y. Wang, W. Chen, and H. Chen, "Dynamics modelling for deep groove ball bearings with local faults based on coupled and segmented displacement excitation," *J. Sound Vib.*, vol. 447, pp. 1–19, May 2019.

[21] H. Cao, L. Niu, S. Xi, and X. Chen, "Mechanical model development of rolling bearing-rotor systems: A review," *Mech. Syst. Signal Process.*, vol. 102, pp. 37–58, Mar. 2018.

[22] A. Chen and T. R. Kurfess, "Signal processing techniques for rolling element bearing spall size estimation," *Mech. Syst. Signal Process.*, vol. 117, pp. 16–32, Feb. 2019.

[23] M. Luo, J. Guo, X. Wu, and J. Na, "An analytical model for estimating spalled zone size of rolling element bearing based on dual-impulse time separation," *J. Sound Vib.*, vol. 453, pp. 87–102, Aug. 2019.

[24] G. Kogan, R. Klein, and J. Bortman, "A physics-based algorithm for the estimation of bearing spall width using vibrations," *Mech. Syst. Signal Process.*, vol. 104, pp. 398–414, May 2018.

[25] L. Cui, J. Huang, F. Zhang, and F. Chu, "HVSRMS localization formula and localization law: Localization diagnosis of a ball bearing outer ring fault," *Mech. Syst. Signal Process.*, vol. 120, pp. 608–629, Apr. 2019.

[26] J. J. Hasan, M. M. M. Islam, and J.-M. Kim, "Acoustic spectral imaging and transfer learning for reliable bearing fault diagnosis under variable speed conditions," *Measurement*, vol. 138, pp. 620–631, May 2019.

[27] D. Wu, H. Wang, T. He, T. Xie, and H. Liu, "Health monitoring on the spacecraft bearings in high-speed rotating systems by using the clustering fusion of normal acoustic parameters," *Appl. Sci.*, vol. 9, pp. 3246–3264, Aug. 2019.

[28] M. Amarnath, V. Sugumaran, and H. Kumar, "Exploiting sound signals for fault diagnosis of bearings using decision tree," *Measurement*, vol. 46, pp. 1250–1256, Apr. 2013.

[29] S. Lu, P. Zheng, Y. Liu, Z. Cao, H. Yang, and Q. Wang, "Sound-aided vibration weak signal enhancement for bearing fault detection by using adaptive stochastic resonance," *J. Sound Vib.*, vol. 449, pp. 18–29, Jun. 2019.

[30] X. T. Bai, Y. H. Wu, K. Zhang, H. T. Shi, and I. C. Rosca, "Investigation on the effects of the ball diameter difference in the sound radiation of full ceramic bearings," *J. Sound Vib.*, vol. 450, pp. 231–250, Jun. 2019.

[31] X. T. Bai, Y. H. Wu, C. Z. Chen, H. P. Yan, and K. Zhang, "Radiation noise of the bearing applied to the ceramic motorized spindle based on the sub-source decomposition method," *J. Sound Vib.*, vol. 410, pp. 35–48, Dec. 2017.

H. T. SHI was born in Fuyang, Anhui, China, in 1982. He received the B.S., M.S., and Ph.D. degrees in control engineering from Northeastern University, Shenyang, China, in 2001, 2005, and 2012, respectively.

He has been a Professor with Faculty of Mechanical Engineering, Shenyang Jianzhu University, Shenyang, since 2013, where he has also been the Vice Dean, since 2014. He is the author of more than 30 articles and five patents. His current research interests include hybrid ceramic ball-bearing dynamic modeling and fault diagnosis.

Prof. Shi was a recipient of the Liaoning Science and Technology Award and the Liaoning Natural Science Achievement Award. He was one of the participants of the prize for scientific and technological progress given by the ministry of education. He was also a common member of the Liaoning Society of Vibration Engineering.

X. T. BAI was born in Wanghua, Fushun, Liaoning, China, in 1989. He received the B.S. degree in mechanical engineering from the Dalian University of Technology, Dalian, Liaoning, in 2011, and the M.S. and Ph.D. degrees in mechanical engineering from the Shenyang University of Technology, in 2013 and 2016, respectively.

He has been a Lecturer with the Faculty of Mechanical Engineering, Shenyang Jianzhu University, Shenyang, since 2016, where he carried out his Postdoctoral Research in the Postdoctoral Station, from 2016 to 2018. He has been a Visiting Scholar with Romania, for three months. He is the author of more than 15 articles and two patents. His current research interest includes the vibration and sound radiation of bearings.

Dr. Bai was a recipient of the Science and Technology Progress Award given by the China Society of Mechanical Engineering and the Liaoning Science and Technology Award. He has been the Deputy Secretary-General and a member of the Liaoning Society of Vibration Engineering, since 2018, and has also been the Reviewer of the *Journal of Sound and Vibration* and *Mechanical Systems and Signal Processing*, since 2019.

K. ZHANG was born in Shenyang, Liaoning, China, in 1969. He received the B.S. and M.S. degrees in mechanical engineering from Shenyang Jianzhu University, Shenyang, in 1992 and 1995, respectively, and the Ph.D. degree in mechanical engineering from Northeastern University, Shenyang, in 2007.

He was a National Visiting Scholar with the Northeast University, Japan, in 2008. He was the Dean of the Faculty of Mechanical Engineering, from 2015 to 2018, where he has been a Professor, since 2006. He has also been the Vice Rector of Shenyang Jianzhu University, since 2018. He is the author of more than 200 articles and six patents. His current research interests include the rotor dynamics of bearings and spindles.

Prof. Zhang was a recipient of the National Technology Invention Award and the National Science and Technology Progress Award. He was awarded as Climbing Scholars of Liaoning Province, in 2018. He has been one of the Yangtze River Scholars, since 2013.

Z. N. WANG was born in Shenhe, Shenyang, Liaoning, China, in 1989. He received the B.S. degree in vehicle engineering from Dalian Jiaotong University, in 2012, and the M.S. degree in mechanical engineering from Shenyang Jianzhu University, China, in 2015, where he is currently pursuing the Ph.D. degree in mechanical engineering.

From 2015 to 2019, he was a Research Assistant with the Key Laboratory of Spindle System of Numerical Control Machine Tool, Liaoning, and a member of the Program for Yangtze Scholars and Innovative Research Team. He is the author of more than 20 patents and more than six articles that were indexed by SCI/EI. His research interests include the development of the spindle magnetic effect, bearing vibration, and TBM techniques optimization.

Mr. Wang was a recipient of the first-class and second-class school scholarships. He is one of the important participants of the National Natural Science Foundation of China and Natural Science Foundation of Liaoning province.

Z. M. LIU was born in Dadong, Shenyang, China, in 1992. He received the bachelor's degree in machinery and automation from Northeastern University, Shenyang, Liaoning, China, in 2015. He is currently pursuing the M.S. degree in mechanical engineering with Shenyang Jianzhu University, China.

His main research interests include fault diagnosis of motorized spindle and fault dynamics of bearing systems, fault dynamics of all-ceramic bearing outer ring, coupling fault dynamics of ceramic motorized spindle, and intermittent fault diagnosis of motorized spindle and rolling bearing.

Mr. Liu was a recipient of the Northeastern University SMC Education Foundation Scholarship and the Shenyang Jianzhu University Entrance Scholarship.